nanomaterials

MDPI

Article

Covalent Triazine Framework C_6N_6 as an Electrochemical Sensor for Hydrogen-Containing Industrial Pollutants. A DFT Study

Hassan H. Hammud [1,*,†], Muhammad Yar [2,†], Imene Bayach [1] and Khurshid Ayub [2,*]

[1] Department of Chemistry, College of Science, King Faisal University, Al-Ahsa 31982, Saudi Arabia
[2] Department of Chemistry, COMSATS University Islamabad, Abbottabad Campus, KPK, Islamabad 22060, Pakistan
* Correspondence: hhammoud@kfu.edu.sa (H.H.H.); khurshid@cuiatd.edu.pk (K.A.)
† These authors contributed equally.

Abstract: Industrial pollutants pose a serious threat to ecosystems. Hence, there is a need to search for new efficient sensor materials for the detection of pollutants. In the current study, we explored the electrochemical sensing potential of a C_6N_6 sheet for H-containing industrial pollutants (HCN, H_2S, NH_3 and PH_3) through DFT simulations. The adsorption of industrial pollutants over C_6N_6 occurs through physisorption, with adsorption energies ranging from −9.36 kcal/mol to −16.46 kcal/mol. The non-covalent interactions of analyte@C_6N_6 complexes are quantified by symmetry adapted perturbation theory (SAPT0), quantum theory of atoms in molecules (QTAIM) and non-covalent interaction (NCI) analyses. SAPT0 analyses show that electrostatic and dispersion forces play a dominant role in the stabilization of analytes over C_6N_6 sheets. Similarly, NCI and QTAIM analyses also verified the results of SAPT0 and interaction energy analyses. The electronic properties of analyte@C_6N_6 complexes are investigated by electron density difference (EDD), natural bond orbital analyses (NBO) and frontier molecular orbital analyses (FMO). Charge is transferred from the C_6N_6 sheet to HCN, H_2S, NH_3 and PH_3. The highest exchange of charge is noted for H_2S (-0.026 e^-). The results of FMO analyses show that the interaction of all analytes results in changes in the $E_{H\text{-}L}$ gap of the C_6N_6 sheet. However, the highest decrease in the $E_{H\text{-}L}$ gap (2.58 eV) is observed for the NH_3@C_6N_6 complex among all studied analyte@C_6N_6 complexes. The orbital density pattern shows that the HOMO density is completely concentrated on NH_3, while the LUMO density is centred on the C_6N_6 surface. Such a type of electronic transition results in a significant change in the $E_{H\text{-}L}$ gap. Thus, it is concluded that C_6N_6 is highly selective towards NH_3 compared to the other studied analytes.

Keywords: industrial pollutants; covalent triazine framework C_6N_6; density functional theory; QTAIM analysis

Citation: Hammud, H.H.; Yar, M.; Bayach, I.; Ayub, K. Covalent Triazine Framework C_6N_6 as an Electrochemical Sensor for Hydrogen-Containing Industrial Pollutants. A DFT Study. *Nanomaterials* **2023**, *13*, 1121. https://doi.org/10.3390/nano13061121

Academic Editor: Shiqiang (Rob) Hui

Received: 7 February 2023
Revised: 7 March 2023
Accepted: 15 March 2023
Published: 21 March 2023

1. Introduction

In the last few decades, industrial pollutants have become serious threats to living beings. Industrial pollutants are adversely deteriorating our ecosystem. It is reported that every year, 4.2 million people are affected by direct exposure to industrial pollutants at levels beyond the safety limits [1]. Among industrial pollutants, hydrogen-containing substances such as HCN, H_2S, NH_3 and PH_3 are highly poisonous to humans [2–5]. Hydrogen cyanide (HCN) is a poisonous gas with an almond-like odour. HCN is used as a reagent for the synthesis of various synthetic fibres, pesticides, plastics and dyes [6]. In cases of contact with skin, ingestion and inhalation, HCN is highly lethal to humans. HCN may cause suffocation, unconsciousness, cramps and heart problems. Hydrogen sulphide (H_2S) is a gas with a rotten egg smell which is usually produced by decomposition of organic materials [7]. It rapidly reacts with the haemoglobin in blood and reduces the

oxygen carrying capacity of vital organs. In addition, the detection and removal of H_2S is particularly essential in petrochemical manufacturing and the coal industry. Another industrially demanding chemical is NH_3, which is a colourless gas with a pungent smell. It is most widely used in the pharmaceutical and fertilizer industries [8,9]. Phosphine is another hydrogen-containing industrial pollutant, which is used to kill insects. In the semiconductor industry, PH_3 is applied in silicon processing [10].

The above-mentioned facts demonstrate the need to design an effective electrochemical sensor for environmental monitoring of these hazardous gases. In the recent past, numerous materials such as ZrO_2 nanoparticles [11], carbon nanotubes [10], metal organic frameworks [11,12], porous silica [13], carbon nitride (C_2N) [13], hexagonal boron nitride [14], metal oxides [15] and zeolites [16] have been tested as adsorbents and gas sensors [12,17]. In addition, nanocages such as aluminium nitride [18], boron nitride [19], carbon nitride [20], metal clusters [21] and phosphorus carbide [22] have been applied as sensors. The essential pre-requisites for any material to act as a sensor are a high selectivity and sensitivity, a fast response, ease of handling, a low hazard to the environment, a high surface to volume ratio and a high recyclability [23,24]. Materials with a large surface to volume ratio can efficiently interact with analytes. The scientific community has developed new materials to overcome the existing limitations of designed materials, such as a low number of active sites, a lack of a tuneable band gap, a low recyclability, a high cost, a low surface area and selectivity and sensitivity issues. Graphene and graphene-doped materials are among the materials used as sensor materials for toxic and hazardous gases [25–29]. The honeycomb-like structure with a large surface area makes graphene an exceptional material for energy storage [23]; photonics [20]; chemical [22], mechanical [30] and DNA sensing [19]; electrocatalysis [2]; electrochemical sensing [31]; and electronic [19] applications. Similarly, other 2D materials such as germanene [32], transition metal dichalcogenides (TMDs) [33], silicene [34–36], phosphorene [37], etc., also offer abundant adsorption sites for separation and sensing of the desired materials. However, the zero band gap of graphene causes a switch off problem in optoelectronic devices [38]. Engineered graphene shows improved electronic charge mobility [39,40]. Many attempts have been made to increase the band gap of graphene through physiochemical engineering. Still, it is not easy to produce a material with a controlled pore size and a suitable band gap [41]. Certainly, the above-mentioned materials have many beneficial characteristics, but their limitations, such as low recyclability, low surface area, low number of active sites and high cost, cannot be ignored. In addition, many surfaces used as sensors contain heavy metals, causing a disposal issue.

Another newly developed class of 2D and 3D materials are covalent organic frameworks, which consist of a variety of organic units as monomers. In 2005, Yaghi et al. synthesized COF1 through a mechanism based on reticular chemistry [42]. Covalent organic frameworks are crystalline porous materials with controlled pore sizes, well-defined surface areas, low densities, light weights and high thermal stabilities. Due to these characteristics, COFs have attracted a lot of interest in various fields of material science, such as solar cells, gas storage, proton conductivity, catalysis, energy storage devices, etc. [43]. In the recent past, several COFs have been utilized as sensors [44] for trinitrotoluene (TNT), picric acid [45], chromium (Cr), arsenic (As) [46,47] and iodine [48]. Previous reports show that covalent triazine frameworks (CTFs) are better sensors compared to COFs due to their controlled porosity, high density nitrogen cavities, high surface areas, high chemical and thermal stabilities, reproducible sensing responses and tuneable electronic properties [49,50]. These characteristics provide suitable conditions for the trapping and detection of analytes and infer the increased potential of CTFs as sensor surfaces compared to COFs. However, CTFs have been studied experimentally as sensors for harmful gases and heavy metals [51–53].

Keeping in view the above-mentioned characteristics of covalent triazine frameworks (CTFs), we selected a recently designed covalent triazine framework (C_6N_6), which contains six nitrogens in its cavity. Recently, C_6N_6 has been used in many fields such as catalysis [54], sensing [55], drug delivery [56] and energy storage [57]. These findings show that the C_6N_6

surface is more comparable to other available COFs for the detection of H-containing industrial pollutants such as HCN, H_2S, NH_3 and PH_3. The high amount of nitrogen in the C_6N_6 unit also leads to a high surface area and a cavity size of 5.46 Å, which can efficiently interact with various analytes through H bonding, π–π stacking or other types of chemical interactions. According to the best of our knowledge, C_6N_6 has not yet been tested as a sensor for the above-mentioned analytes. In the designed study, we used density functional theory simulations to investigate C_6N_6 as a sensor surface. Changes in geometrical properties are explored through NCI, QTAIM and SAPT0 analyses, while changes in the electronic properties of analytes in C_6N_6 complexes are determined by NBO, EDD and FMO analyses.

2. Computational Methodology

Gaussian 09 software was used to carry out the simulations in the current study. The selected geometries of bare C_6N_6 and analyte@C_6N_6 complexes were investigated at the ωb97XD/6-31G (d, p) level of theory. The ωb97XD functional was adopted in the current study because it is a range-separated functional which can effectively capture non-localized intermolecular interactions [58]. In ωb97XD, the symbol "ω" represents the long range correction [59]. Additionally, the ωb97XD functional also contains Grimme's D2 dispersion factor to efficiently study the van der Waals (vdWs) interactions [59]. The changes in the electronic properties of C_6N_6 before and after adsorption of analytes were explored by NBO, EDD and FMO analyses at the B3LYP/6-31G(d) level of theory. B3LYP/6-31G(d) is considered as the best to study the electronic changes of interacted systems [60–65]. The most stable configurations of the analyte@C_6N_6 complexes were investigated by adsorption of analytes through different orientations of C_6N_6. A frequency analysis was performed to confirm that the geometries of the complexes were true minima on the potential energy surface. The energies of adsorbed analytes in C_6N_6 are determined by Equation (1):

$$\Delta E = [E_{(analytes@C6N6)} - (E_{C6N6} + E_{analytes})] \quad (1)$$

where $E_{(analytes@C6N6)}$ is the interaction energy of the complexes, E_{C6N6} is the energy for bare C_6N_6 and $E_{analytes}$ is the energy of the industrial pollutants used as analytes.

A SAPT0 analysis was applied to determine the role of the individual components of the interaction energy in the stabilization of the analyte@C_6N_6 complexes [66]. The total SAPT0 energy is the sum of four factors: induction (ΔE_{ind}), dispersion (ΔE_{disp}), electrostatic (ΔE_{elstat}) and exchange (ΔE_{exch}). Hence, the SAPT0 energy is calculated through Equation (2):

$$\Delta E_{SAPT0} = \Delta E_{elstat} + \Delta E_{exch} + \Delta E_{ind} + \Delta E_{disp} \quad (2)$$

The nature of adsorption, such as the electrostatic, dispersive and repulsive forces between the analyte and C_6N_6, was examined by an NCI analysis. The nature and strength of non-covalent interactions is given by the reduced density (s), Equation (3) [67].

$$s = \frac{1}{2(3\pi^2)^{\frac{1}{3}}} \frac{\nabla\rho}{\rho^{4/3}} \quad (3)$$

The value of electron density *(ρ)* for non-covalent interactions is generally very small. However, small changes in *(ρ)* result in prominent changes in RDG values, which appear in the form of spikes in a 2D-RGD plot. An NCI analysis characterizes non-covalent interactions through 3D-isosurfaces and 2D-RGD plots. These plots use ρ and the second eigen value (λ_2) to differentiate between the nature of interactions [68–70].

The interaction between the analytes and C_6N_6 was further studied through a QTAIM analysis. Through a QTAIM analysis, we can examine the nature of the interactions, which cannot be explored through any other method. The major factor through which non-covalent interactions can be studied through QTAIM analysis is the bond critical point (BCP). BCPs are based on various parameters such as the Laplacian ($\nabla^2\rho$), electron density

(ρ), total energy density (H), potential energy density (V) and the Lagrangian kinetic energy density (G) [71–73]. Multiwfn 3.7 and VMD software were used to perform the QTAIM, NCI and EDD analyses [74–76].

3. Results and Discussion

3.1. Geometry Optimization and Interaction Energy

The optimized structure of the selected model of C_6N_6 is presented in Figure 1. The C-C and C-N bond lengths in C_6N_6 are 1.53 Å and 1.33 Å, respectively, which are consistent with previously reported theoretical and experimental values [77]. Each unit of C_6N_6 comprises of six C_3N_3 rings which are connected with each other through C-N bonds [55]. The cavity of the selected model of C_6N_6 has a high electron density due to the centring of the nitrogen atoms towards the cavity. The diameter of the C_6N_6 cavity (between two nitrogen atoms) is 5.46 Å [78]. The nitrogenated, high electron density cavity of C_6N_6 can act as a potential surface for the detection of hydrogen-containing industrial pollutants. The topologies of selected industrial pollutants (HCN, H_2S, NH_3 and PH_3) were also simulated at the ωb97XD/6-31G (d, p) level.

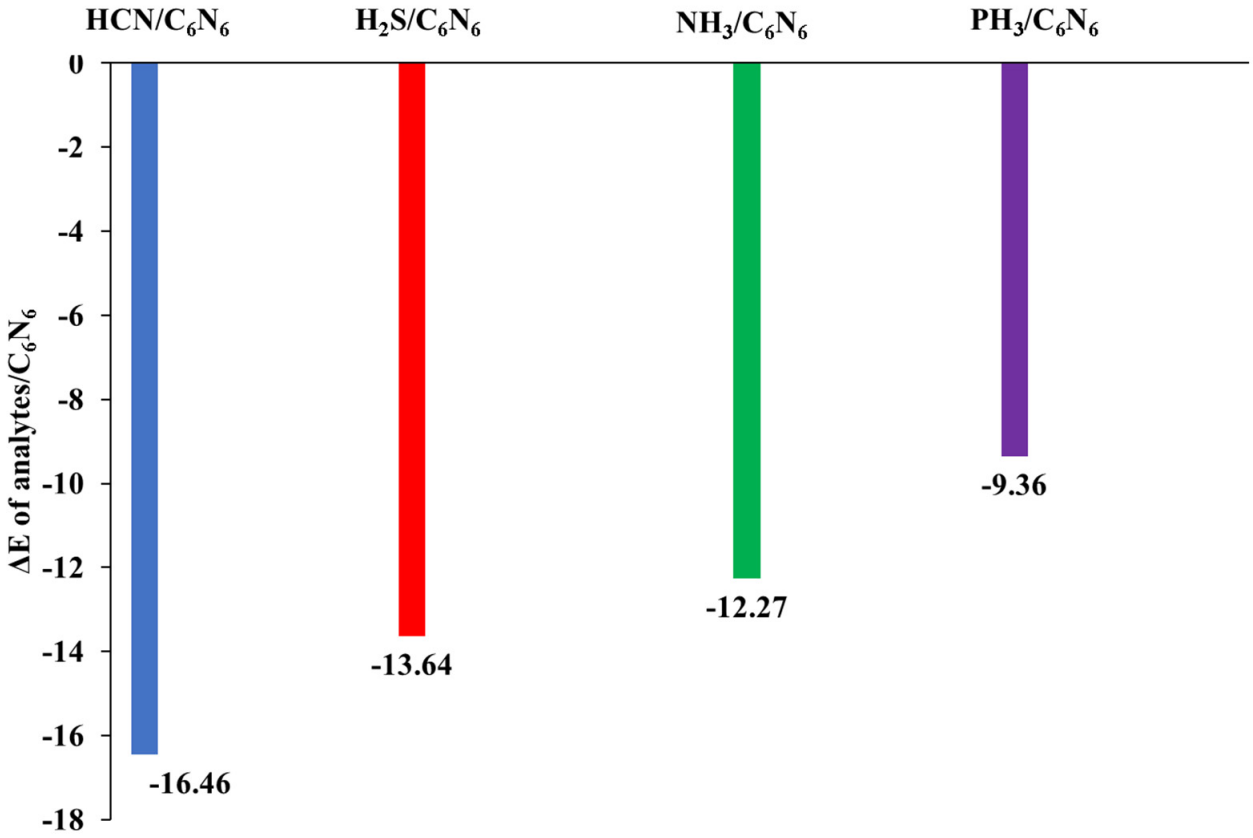

Figure 1. Graphical representation of adsorption energies of analyte@C_6N_6 complexes at the ωb97XD/6-31G (d,p) level of theory.

In order to obtain stable complexes of analyte@C_6N_6, several orientations of each analyte in C_6N_6 were considered. Figure 1 shows a graphical representation of the adsorption energies of analyte@C_6N_6 complexes. The most stable geometries of each analyte@C_6N_6 complex are reported in Figure 2, while the remaining geometries are given in Figure S1 (Supplementary Materials). The following order of the adsorption energies of the stable complexes is obtained: HCN@C_6N_6 > H_2S@C_6N_6 > NH_3@C_6N_6 > PH_3@C_6N_6.

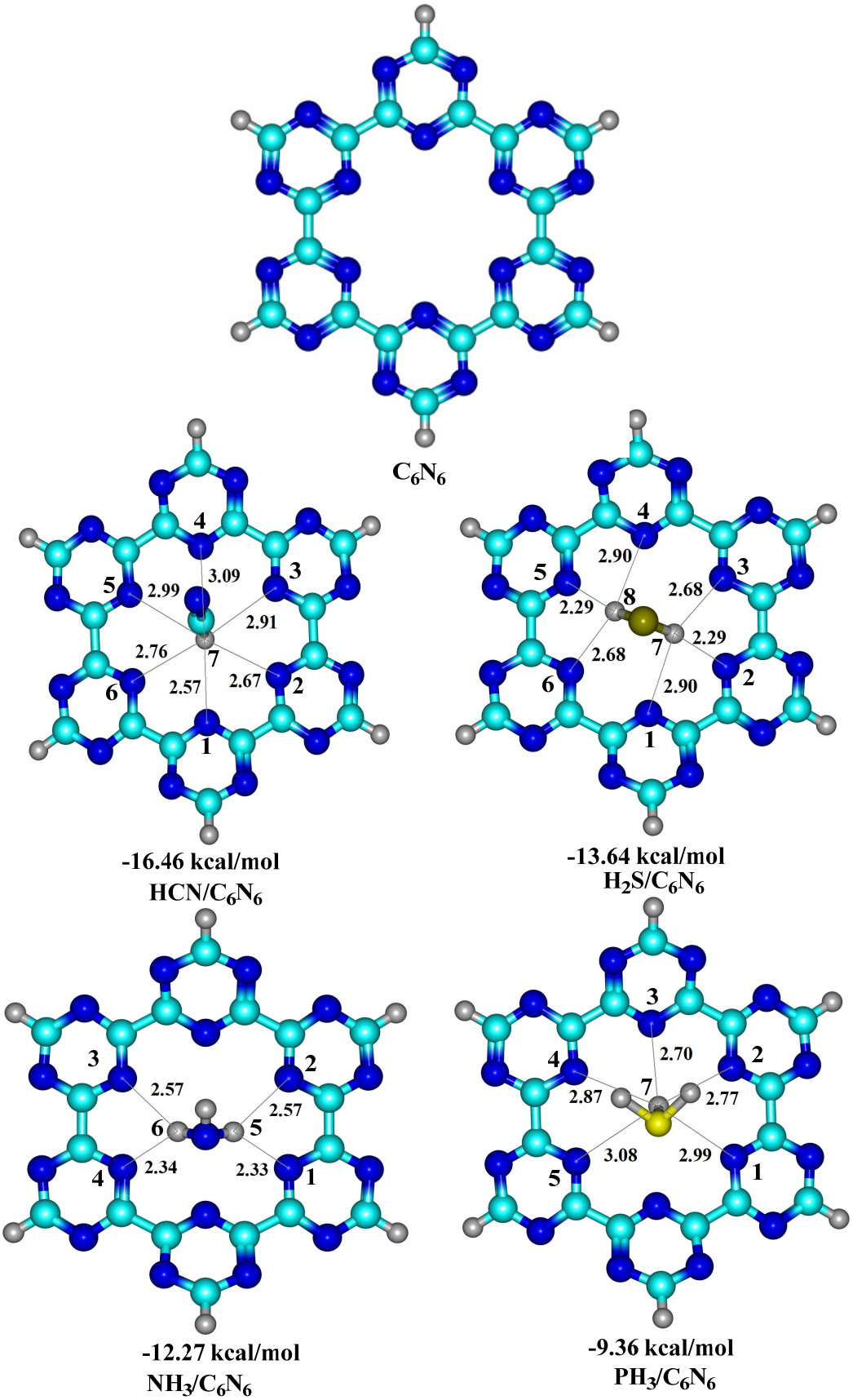

Figure 2. Top view of optimized structures of the analyte@C_6N_6 complexes at the ωb97XD/6-31G (d,p) level of theory.

Among the analyte@C_6N_6 complexes, the most stable complex is formed between HCN and C_6N_6, with an adsorption energy value of −16.46 kcal/mol. In this complex, HCN is projected to be perpendicular to the C_6N_6 cavity (see Figure 2). The H atom of HCN interacts with the N atoms of C_6N_6 at bond distances of between 2.57 Å and 3.09 Å. Among these interactions, the strongest interaction is seen between the H7 atom of HCN and the N1 and N2 of C_6N_6, with interaction distances of 2.57 Å and 2.67 Å, respectively. These interaction distances show that HCN is more attracted to the two C_3N_3 rings containing N1 and N2 atoms. When the input geometry was altered to have the nitrogen atom of HCN pointing towards the cavity of C_6N_6, the calculation converged to the same complex mentioned above (hydrogen pointing towards the cavity). This happened because of the repulsion between the N atom of HCN and the N atoms of C_6N_6.

The stable complex of H_2S@C_6N_6 is obtained with an adsorption energy of −13.64 kcal/mol, which is the 2nd most stable complex among all studied analyte@C_6N_6 complexes. The optimized topology of the H_2S@C_6N_6 complex shows that both H atoms of H_2S are positioned towards the C_6N_6 cavity. Interaction distances of 2.90 Å (N1—H7), 2.29 Å (N2—H7) and 2.68 Å N2—H7 are noted between N atoms (N1, N2 and N3) of C_6N_6 and the H atom (H7) of H_2S (see Figure 2). Moreover, similar interaction distances are observed between N4—H8, N5—H8 and N6—H8, respectively. However, these interaction distances between the N atoms of C_6N_6 and the H atoms of H_2S reveal that the adsorption of H_2S occurred at the centre of cavity, while the S atom is pointing upwards.

The stable complex of NH_3@C_6N_6 resulted in an adsorption energy of −12.27 kcal/mol, which is slightly lower than that of the H_2S@C_6N_6 complex. In the stable configuration of NH_3@C_6N_6, two H atoms of NH_3 interact with the N atoms of C_6N_6, while the 3rd H atom is projected away from the cavity. Among the observed interactions, strong interactions are observed between N1 and H5 and N4 and H6 of C_6N_6 and H_2S, with distances of 2.33 Å and 2.34 Å, respectively. The N2 and N3 of C_6N_6 interact with H5 and H6 of NH_3, with an interaction distance of 2.57 Å. The lower adsorption energy of the NH_3@C_6N_6 complex (−12.27 kcal/mol) compared to the H_2S@C_6N_6 complex (−13.64 kcal/mol) is attributed to longer interaction distances between the H atoms of NH_3 and the N atoms of C_6N_6 compared to H_2S.

An adsorption energy of −9.36 kcal/mol is observed for the stable complex of PH_3@C_6N_6, which is the lowest amongst all studied analyte@C_6N_6 complexes. The stable structure of the PH_3@C_6N_6 complex consists of an inward pointing H atom of PH_3, while the other two H atoms point upwards. The inward pointing H atom of PH_3 is almost at the centre of the C_6N_6 cavity. The bond distances between the H atoms of PH_3 and the N atoms of C_6N_6 range from 2.70 Å to 3.09 Å. The low adsorption energy (−9.36 kcal/mol) of the PH_3@C_6N_6 complex is due to the low polarity of the H atoms of PH_3 and the longer interaction distances. The results of adsorption energies (−9.36 kcal/mol to −16.46 kcal/mol) show all analytes (HCN, H_2S, NH_3 and PH_3) physically absorb on the C_6N_6 sheet.

3.2. Symmetry Adapted Perturbation Theory (SAPT0) Analysis

A SAPT0 analysis is the most effective method for quantifying non-covalent interactions. The SAPT0 interaction energy is the sum of four factors, including induction, exchange, electrostatic and dispersion. Therefore, in SAPT0, the role of each factor is investigated in the stabilization of analytes in C_6N_6. The SAPT0 results of all the studied complexes are presented in Table 1 and Figure 3. In the SAPT0 graph, five bars are shown for each complex. The last green bar represents the total SAPT0, which is the sum of the first four bars. Out of these four bars, three bars with negative signs indicate attractive interactions, while the bars with +ve signs indicate repulsive interactions. The negative sign of the green bar (total SAPT0) reveals the dominance of attractive forces over repulsive forces during the interaction of analytes with the C_6N_6 sheet.

Table 1. Stabilization energies of analyte@C_6N_6 complexes obtained through SAPT0 analyses.

Analytes@C_6N_6	E_{exch}	E_{elst}	(%)	E_{ind}	(%)	E_{disp}	(%)	E_{SAPT0}
HCN@C_6N_6	11.16	−14.60	(52)	−3.78	(13)	−9.66	(34)	−16.88
H_2S@C_6N_6	16.93	−12.58	(43)	−4.27	(15)	−12.34	(42)	−12.26
NH_3@C_6N_6	25.29	−10.78	(47)	−2.93	(13)	−9.30	(40)	−10.06
PH_3@C_6N_6	11.77	−6.85	(33)	−2.54	(12)	−11.60	(55)	−9.22

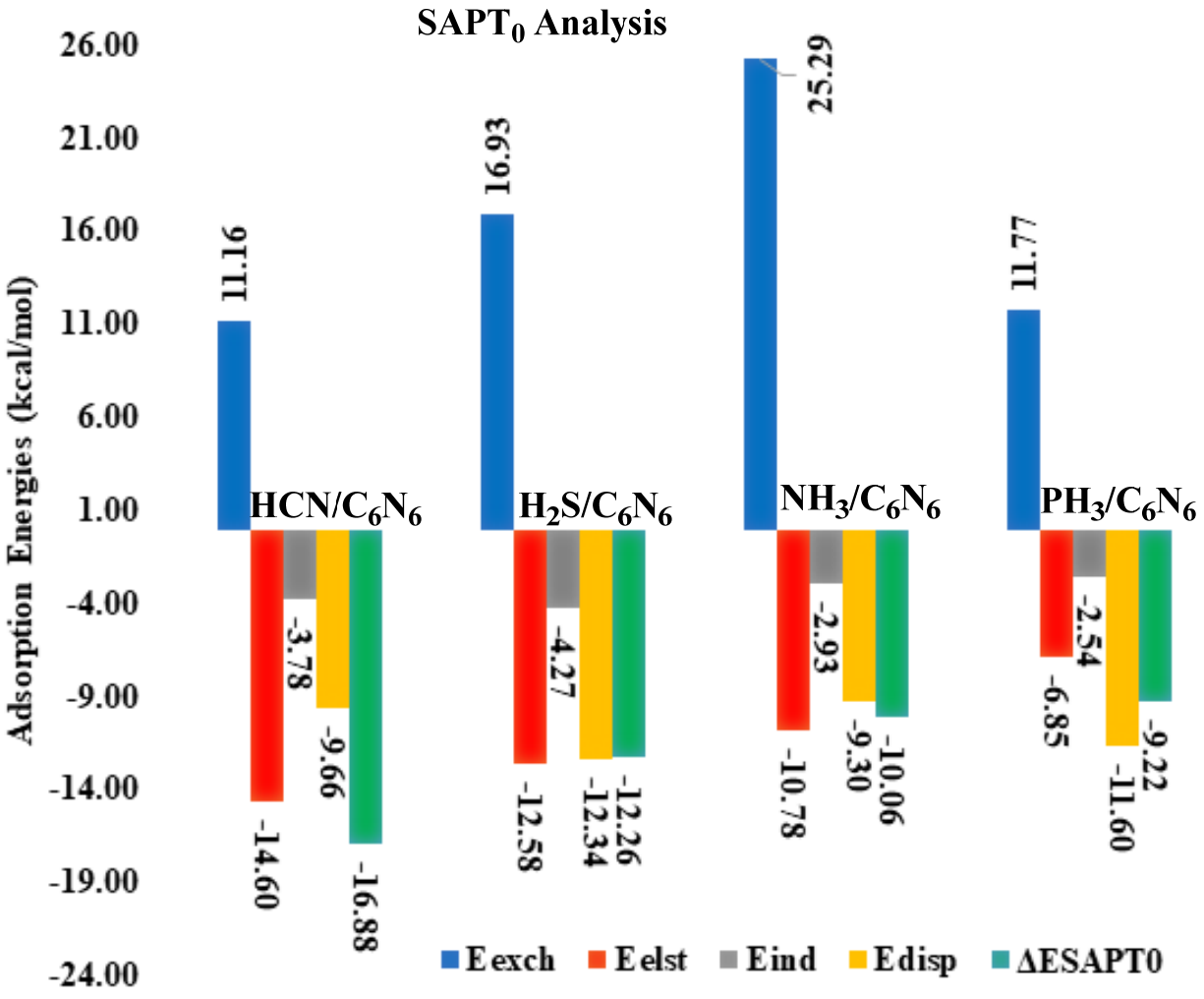

Figure 3. Graphical projection of the SAPT0 energy and its components for analyte@C_6N_6 complexes.

The SAPT0 energies of all the complexes obtained through PSI4 are −16.88 kcal/mol (HCN@C_6N_6), −12.26 kcal/mol (H_2S@C_6N_6), −10.06 kcal/mol (NH_3@C_6N_6) and −9.22 kcal/mol (PH_3@C_6N_6). Among the studied H-containing industrial pollutants over C_6N_6, the highest SAPT0 value (−16.88 kcal/mol) is obtained for the HCN@C_6N_6 complex, which is consistent with the results of the interaction energy analysis. The SAPT0 attractive component values for the HCN@C_6N_6 complex are E_{elst} (−14.60 kcal/mol: 52%), E_{ind} (−3.78 kcal/mol: 13%) and E_{disp} (−9.66 kcal/mol: 34%). These values indicate that E_{elst} is the major stabilizing factor compared to E_{ind} and E_{disp}. The highest value of E_{elst} results from the strong interactions of the H atom of HCN with the N atoms of C_6N_6 through a shorter interaction distance (vide supra).

The second highest SAPT0 value is seen for the H_2S@C_6N_6 complex, at −12.26 kcal/mol. The energy values of the attractive components, i.e., E_{elst}, E_{ind} and E_{disp}, observed for the H_2S@C_6N_6 complex are −12.58 kcal/mol (43%), −4.27 kcal/mol (15%) and −12.34 kcal/mol

(42%), respectively. These values of the attractive components show that E_{elst} (43%) and E_{disp} (42%) play a major role in the stabilization of the $H_2S@C_6N_6$ complex, while a lower contribution is observed for E_{ind} (15%). The SAPT0 values for the $NH_3@C_6N_6$ and $PH_3@C_6N_6$ complexes are −10.06 kcal/mol and −9.22 kcal/mol, respectively. The SAPT0 component analysis for the $NH_3@C_6N_6$ complex reveals that E_{elst} (47%) and E_{disp} (40%) are dominant in the stabilization of NH_3 over C_6N_6. Among the studied pollutant complexes, the lowest SAPT0 value is observed for the $PH_3@C_6N_6$ complex (−9.22 kcal/mol). The lowest SAPT0 value for the $PH_3@C_6N_6$ complex results from the lower polarity of the interacting H atoms of PH_3 with the N atoms of C_6N_6. Among the SAPT0 energy, a key role is noted for E_{disp} (55%) in the stabilization of the $PH_3@C_6N_6$ complex, while E_{elst} (33%) and E_{ind} (12%) contribute less towards the total SAPT0 energy.

The SAPT0 analysis reveals that E_{elst} is the dominant contributing factor in the case of $HCN@C_6N_6$, whereas a good balance between E_{elst} and E_{disp} is observed for H_2S and NH_3. In the case of PH_3, the dispersion interaction played a dominant role in the stabilization of PH_3 over C_6N_6. The SAPT0 values of all the studied complexes are consistent with the interaction energy analysis.

3.3. Non-Covalent Interaction (NCI) Analysis

The nature of interactions between analytes and C_6N_6 was further explored through non-covalent interaction analyses. Through an NCI analysis, the van der Waals, electrostatic and repulsive interactions can be differentiated based on a colour scheme. An NCI analysis comprises 3D isosurfaces and 2D reduced density gradient (RDG) plots. The 3D isosurface topological analysis is based on three types of colours: red (repulsive), green (van der Waals) and blue (electrostatic interactions). These colours appear in the form of patches between the analytes and C_6N_6 through which the nature of interactions can be differentiated. A 2D RDG plot is obtained by taking the reduced density on the *Y*-axis and product of 2nd value of the Laplacian (sign(λ_2)) and density gradient on the *X*-axis. A 2D RGD plot gives information about the strength of each type of interaction. In 2D RDG plots, non-covalent interactions appear as blue, green and red spikes in the low density gradient region. The vdWs interactions are indicated by the green spikes which form the when product of sign(λ_2)ρ is in the range of −0.00 a.u. to −0.02 a.u. A large and negative value of the product of sign(λ_2)ρ (above −0.02 a.u.) signifies the existence of electrostatic interactions (blue spikes). Red spikes in the 2D-RGD plot show repulsive interactions when the product of sign(λ_2)ρ is positive and large.

The topologies obtained through NCI analyses are presented in Figure 4. In the studied complexes, the green spikes in the 2D RDG plots and the green isosurface in the 3D plots are explored. The green spikes and isosurface indicate vdWs interactions between the analytes and C_6N_6. The strength of the vdWs interaction in each complex is different, indicated by the variation in the thickness of 3D isosurface patches and a projection of green spikes in the 2D-RDG plots on the *X*-axis. In the case of the $HCN@C_6N_6$ complex, a ring on the green isosurface develops between the H atom of HCN and the six N atoms of C_6N_6. This shows that all six N atoms of C_6N_6 strongly interact with the H atom of HCN. Similarly, in the 2D-RDG plot, a mixture of bluish-green spikes arises at a low-density gradient between −0.01 and −0.02 a.u., which indicates that the complex is stabilized through electrostatic interactions. In the case of the $H_2S@C_6N_6$ complex, a stronger interaction is observed, where the H atoms of H_2S closely interact with the N atoms of C_6N_6 (see Figure 4). The rest of the interactions are present at longer distances due to the angular orientation of the H_2S molecule over C_6N_6. The 3D isosurfaces and 2D-RGD plots of the $NH_3@C_6N_6$ complex reveal the weak interaction compared to the $HCN@C_6N_6$ and $H_2S@C_6N_6$ complexes. The scattered green spikes and shattered green isosurface in the 3D NCI plots are due to the weak interaction between NH_3 and the C_6N_6 cavity. The weak interaction of NH_3 is also described in the interaction energy section. In the case of the $PH_3@C_6N_6$ complex, the green spikes and isosurface are not as thick and dense as projected in the rest of the studied complexes. Out of the three hydrogens atoms of PH_3, only one H is oriented towards the

C_6N_6 cavity. The H atom orientated towards the C_6N_6 cavity is not as polar as the H atom of HCN and NH_3, due to which weak vdWs interactions are established between PH_3 and the C_6N_6 cavity. The NCI analysis indicated that dispersion and electrostatic interactions are dominant, which is consistent with the SAPT0 and interaction energy results.

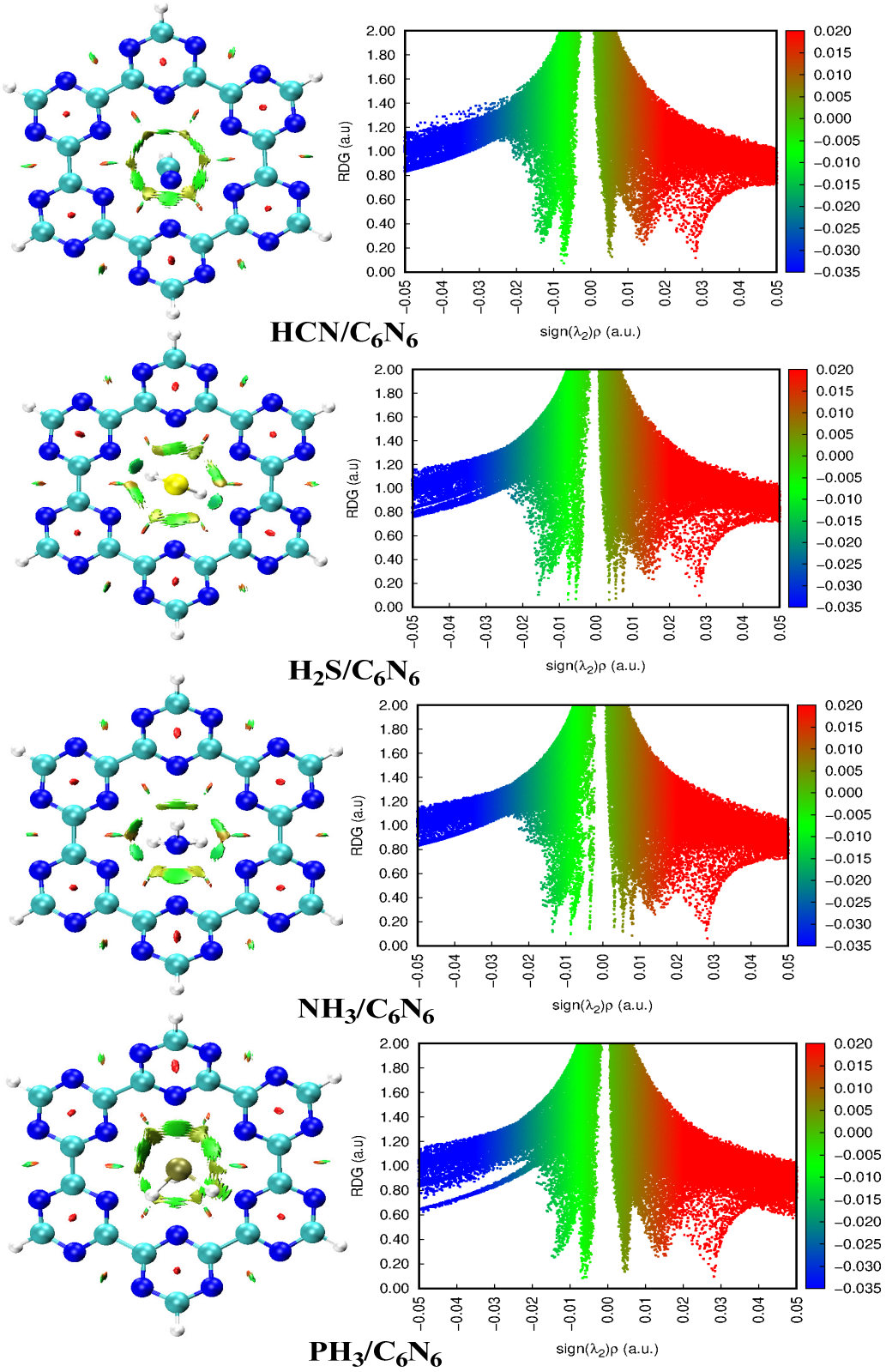

Figure 4. NCI analyses of analyte@C_6N_6 complexes at an iso-value of 0.002 a.u.

3.4. Quantum Theory of Atoms in Molecule (QTAIM) Analysis

QTAIM analysis is a useful tool to investigate all non-covalent interactions which are impossible to capture through any other analysis. Through QTAIM analysis, inter- and intra-molecular interactions such as ionic interactions, hydrogen bonding, van der Waals interactions and covalent bonds can be studied. These inter- and intra-molecular interactions are studied by various parameters such as cage critical points (CCP), nuclear critical points (NCP), ring critical points (NCP) and bond critical points (BCPs). In QTAIM analyses, non-covalent interactions are best explained by BCPs. BCPs between two interacting systems are represented by a brown line (see Figure 5). The nature and strength of each BCP is explained through several parameters such as ($\nabla^2\rho$), (ρ), (H), (G) and (V). The values of the BCP parameters of all complexes are given in Table 2.

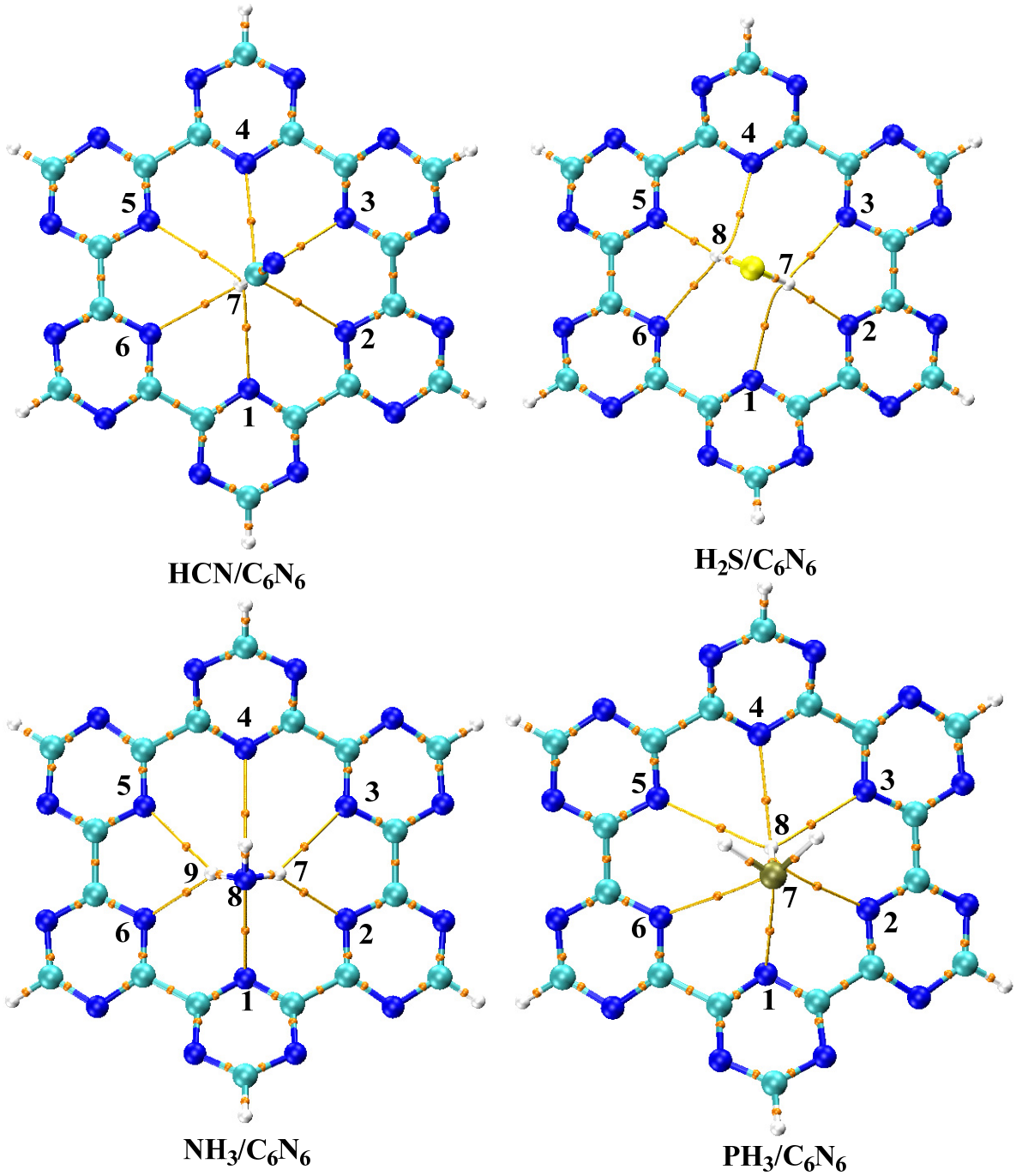

Figure 5. Topological analysis of analyte@C_6N_6 complexes obtained through QTAIM analysis.

Table 2. BCP parameters values of analyte@C_6N_6 complexes determined by QTAIM analyses.

Analyte@C_6N_6	Analyte-C_6N_6	ρ	$\nabla^2\rho$	G (r)	V (r)	H (r)	V(r)/G(r)	Eint (kcal/mol)
HCN@C_6N_6	H7-N1	0.00724	0.02687	0.00540	−0.00408	0.00132	−0.76	−1.28
	H7-N2	0.00706	0.02429	0.00494	−0.00381	0.00113	−0.77	−1.19
	H7-N3	0.00780	0.02622	0.00547	−0.00439	0.00108	−0.80	−1.38
	H7-N4	0.00735	0.02451	0.00508	−0.00404	0.00104	−0.79	−1.27
	H7-N5	0.00659	0.02509	0.00489	−0.00352	0.00138	−0.72	−1.10
	H7-N6	0.00814	0.02847	0.00597	−0.00483	0.00115	−0.81	−1.51
H_2S@ C_6N_6	H7-N1	0.00549	0.01895	0.00380	−0.00285	0.00000	−0.75	−0.90
	H7-N2	0.01586	0.03965	0.00992	−0.00992	0.00000	−1.00	−3.11
	H8-N3	0.00763	0.02552	0.00536	−0.00434	0.00102	−0.81	−1.36
	H8-N4	0.00549	0.01895	0.00379	−0.00285	0.00094	−0.75	−0.89
	H8-N5	0.01585	0.03963	0.00991	−0.00991	0.00000	−1.00	−3.11
	H7-N6	0.00763	0.02552	0.00536	−0.00434	0.00102	−0.81	−1.36
NH_3@C_6N_6	N8-N1	0.00773	0.02558	0.00573	−0.00506	0.00067	−0.88	−1.59
	H7-N2	0.01365	0.04227	0.00991	−0.00925	0.00066	−0.93	−2.90
	H7-N3	0.00867	0.02856	0.00627	−0.00540	0.00087	−0.86	−1.69
	N8-N4	0.00357	0.01222	0.00261	−0.00217	0.00044	−0.83	−0.68
	H9-N5	0.00874	0.02871	0.00631	−0.00545	0.00087	−0.86	−1.71
	H9-N6	0.01360	0.04224	0.00989	−0.00922	0.00067	−0.93	−2.89
PH_3@C_6N_6	P7-N1	0.00687	0.02064	0.00445	−0.00374	0.00071	−0.84	−1.17
	H8-N2	0.00562	0.01924	0.00390	−0.00300	0.00091	−0.77	−0.94
	H8-N3	0.00673	0.02215	0.00456	−0.00358	0.00098	−0.79	−1.12
	H8-N4	0.00730	0.02305	0.00482	−0.00388	0.00094	−0.80	−1.22
	H8-N5	0.00601	0.02070	0.00416	−0.00315	0.00101	−0.76	−0.99
	H7-N6	0.00625	0.02024	0.00435	−0.00365	0.00071	−0.84	−1.14

The nature of interaction is shared if $\nabla^2\rho(r) < 0$, whereas for close shell interactions, the value of $\nabla^2\rho(r) > 0$. For electrostatic interactions (H bonding), the values of ($\nabla^2\rho$) and (ρ) at BCPs are between 0.024 and 0.139 a.u. and 0.002 to 0.034 a.u., respectively [79,80]. In addition, a bond distance (N—H, O—H and F—H) of less than 1.2 Å indicates a strong interaction, while a bond distance greater than 1.8 Å shows a weak interaction [81]. The strength of an individual bond can also be characterized by the Espinosa approach, as presented in Equation (4) [82]. For H bonding, the energy value of an individual bond is >3 kcal/mol (in negative) [83].

$$E_{int}\ (a.u.) = \frac{1}{2}V(r) \quad (4)$$

In addition, the BCP can further be investigated by Equation (5):

$$H(r) = G(r) + V(r) \quad (5)$$

where G, H and V are the kinetic, potential and total energy density at the BCPs, respectively. For close shell interactions, the value of H is usually positive, while it is negative for shared shell interactions. The type of bonding is generally indicated by $\nabla^2\rho$ and H. The values of $\nabla^2\rho$ and H are less than zero for shared shell interactions and greater than zero for close shell interactions. If the values of $\nabla^2\rho$ are greater than zero and H is less than zero, it indicates H bonding. Another parameter used to explain the BCP is the ratio -V/G. If the ratio of -V/G is >2, it indicates covalent bonding, and a ratio of −V/G of < 1 represents non-covalent interactions [84,85].

QTAIM analyses of all the complexes shows that number of BCPs is six in each case due to interactions of six N atoms in the C_6N_6 cavity with the H atoms of interacting analytes. However, the strengths and types of bonding in all complexes are different due to the different values of their BCP parameters (see Table 2). In the case of the HCN@C_6N_6 complex, the $\nabla^2\rho$ and ρ values are in the range of 0.02429 a.u. to 0.0284 a.u. and 0.00706 a.u. to 0.00814 a.u., respectively. The most stable interaction is observed between H7 of HCN and N6 of C_6N_6. The values of $\nabla^2\rho$ and ρ at BCPs between H7 and N6 are 0.0284 a.u. and 0.00814 a.u., respectively. In addition, the rest of the BCP parameter values of the HCN@C_6N_6 complex are in the range of electrostatic attractions, which is consistent with the SAPT0 analysis, where the dominant contribution was electrostatic. The other BCP parameters such as G, H, V, -V/G and E_{int} are in the range of electrostatic interactions.

A topological analysis of the H_2S@C_6N_6 complex also shows six BCPs. Among these BCPs, two BCPs (H7—N2 and H8—N5) are in the strong electrostatic region, while the rest of the BCPs indicate dispersion interactions (see Table 2). Again, the results of the QTAIM analysis for the H_2S@C_6N_6 complex are well matched with the SAPT0, where a good balance between electrostatic and dispersion interactions was observed. The highest values of $\nabla^2\rho$ (0.03965), ρ (.01586 a.u), H (0.00 a.u.) and E_{int} (−3.11 kcal/mol) are observed for H7—N2 and H8—N5, respectively. The BCP parameter such as $\nabla^2\rho$, ρ and E_{int} of H7—N2 and H8—N5 are in the range of H bonding, but no such types of blue isosurface and spikes are seen in the 3D isosurfaces and 2D-RGD plots of NCI analysis. The interaction distances between H7 and N2 and H8 and N5 are 2.29 Å each, which is greater than the 1.8 Å required for interacting system to demonstrate H bonding [81].

The BCP parameter values of the NH_3@C_6N_6 complex are in the range of medium to strong interactions between NH_3 and C_6N_6. The strongest interactions are observed between H7 and N2 and H9 and N6 of NH_3 and C_6N_6, respectively. The values of these two BCP parameters $\nabla^2\rho$, ρ and E_{int} are almost comparable (see Table 2). The values of the rest of the five BCPs indicate vdWs interactions. The number of BCPs for the PH_3@C_6N_6 complex are equal in number with other complexes. However, all BCP parameter values between the H atoms of PH_3 and the N atoms of C_6N_6 are in the range of dispersion interactions, which is consistent with the SAPT0 interaction energy analysis, where PH_3@C_6N_6 was the least stable complex. In all studied analyte@C_6N_6 complexes, the values of BCP parameters are in good agreement with NCI and SAPT0 analyses.

4. Electronic Properties

4.1. Natural Bond Orbital (NBO) and Electron Density Differences (EDD) Analyses

The electronic properties of complexes were explored by EDD and NBO analyses. Through these analyses of the nature of interactions, the stability, charge transfer and sensing ability of the designed surface for selected analytes can be explored. An EDD plot is obtained by subtracting the charges of individual fragments from the charge of the analyte@C_6N_6 complex. The topologies obtained through EDD analyses show two types of isosurface: yellow and green. The yellow surfaces reveal a depletion in charge, while a green colour illustrates an accumulation of charge. Among the studied complexes, both types of isosurface are observed in the adsorption site of analytes and the C_6N_6 surface, which indicates an exchange of electronic charge between them. The topologies of the complexes determined through EDD analyses are presented in Figure 6. In addition, the NBO charge values of each analyte over C_6N_6 are also displayed in Figure 6.

The charge transfer values from C_6N_6 to the analytes are −0.019 e^- (HCN), −0.026 e^- (H_2S), −0.015 e^- (NH_3) and −0.008 e^- (PH_3). These values of charges show that the analytes extracted charge from C_6N_6. In all studied analytes, the H atoms of analytes interacted with the electron rich cavity of C_6N_6, due to which charge is transferred from C_6N_6 to the analytes. The highest charge value is extracted by H_2S (−0.026 e^-) due to a close interaction of the H atoms of H_2S with the N atoms of C_6N_6. Similarly, the accumulation and depletion of electron density in the interacting sites of C_6N_6 and H_2S clearly indicate that the nitrogen of C_6N_6 transferred more charge towards H_2S. In the case

of HCN, a charge of −0.019 e^- is determined, which is contrary to its interaction energies. The EDD analysis of HCN adsorption over C_6N_6 shows that charge is transferred from the N atoms of C_6N_6 to the H atom of HCN. However, the lowest values of charge are observed in NH_3 (−0.015 e^-) and PH_3 (−0.008 e^-) due to the weak interactions of these analytes with the C_6N_6 sheet.

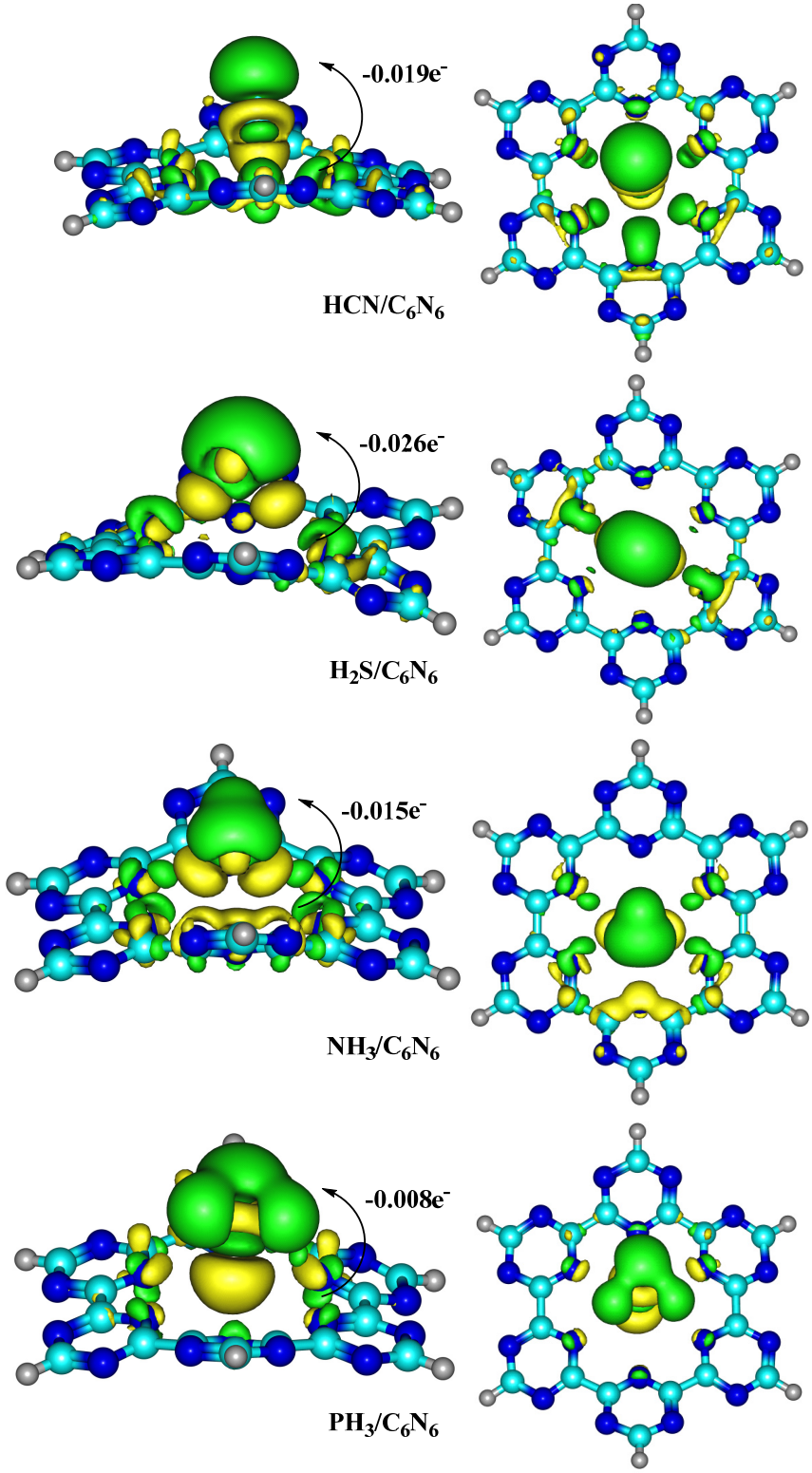

Figure 6. The topologies of analyte@C_6N_6 complexes determined through EDD analysis (Isovalue = 0.0019 a.u.).

4.2. Frontier Molecular Orbital (FMO) Analysis

The electrical signal produced by an electrochemical sensor mainly depends on changes in its electronic properties after interaction with an analyte. To explore these changes in electronic properties of sensors, a frontier molecular orbital analysis was performed. The energy values determined from an FMO analysis of bare C_6N_6 and analyte@C_6N_6 complexes are shown in Table 3. The densities of HOMO and LUMO orbitals are presented in Figure 7. The energies of the HOMO and LUMO for C_6N_6 are −7.16 eV and −3.30 eV, respectively, with a HOMO–LUMO energy gap ($E_{H\text{-}L}$ gap) of 3.86 eV. The interaction of selected industrial pollutants with C_6N_6 causes prominent changes in the energy levels of the HOMO, LUMO and $E_{H\text{-}L}$ gap. The computed values of the $E_{H\text{-}L}$ gaps of HCN@C_6N_6, H_2S@C_6N_6, NH_3@C_6N_6 and PH_3@C_6N_6 complexes are 4.02 eV, 2.76 eV, 2.58 eV and 3.35 eV, respectively.

Table 3. The energies of the HOMO, LUMO and HOMO–LUMO energy gap (EH–L gap) of analyte@C_6N_6 complexes.

Analyte@C_6N_6	HOMO (eV)	LUMO (eV)	Gap
C_6N_6	−7.16	−3.30	3.86
HCN@C_6N_6	−7.43	−3.41	4.02
H_2S@C_6N_6	−6.07	−3.31	2.76
NH_3@C_6N_6	−5.85	−3.27	2.58
PH_3@C_6N_6	−6.62	−3.27	3.35

The results presented in Table 3 show that adsorption of H_2S, NH_3 and PH_3 on C_6N_6 causes a pronounced increase in the HOMO energy, while the LUMO energy of these complexes remains almost unchanged. However, adsorption of HCN shows the inverse behaviour, where a significant decrease in the HOMO energy (−7.43 eV) is noticed compared to C_6N_6 (−7.16 eV). A more pronounced decrease in the HOMO energy causes an increase in the $E_{H\text{-}L}$ gap (4.02 eV) of the HCN@C_6N_6 complex compared to bare C_6N_6 (3.86 eV). This increase in the $E_{H\text{-}L}$ gap of the HCN@C_6N_6 complex indicates a decrease in the conductivity of C_6N_6. As a result, C_6N_6 cannot act as a good sensor for HCN.

Adsorption of H_2S onto C_6N_6 resulted in a prominent increase in the energy of the HOMO (−6.07 eV), while the LUMO energy (−3.31 eV) is almost comparable to bare C_6N_6 (−3.30 eV). This increase in the HOMO energy resulted in a pronounced reduction in the $E_{H\text{-}L}$ gap (2.76 eV) of the H_2S@C_6N_6 complex. Among the different industrial pollutants adsorbed on C_6N_6, the most significant increase in electrical conductivity is observed for the NH_3@C_6N_6 complex due to an appreciable decrease in the $E_{H\text{-}L}$ gap. The energies of the HOMO and LUMO for the NH_3@C_6N_6 complex are 5.85 eV and −3.27 eV, respectively. The interaction of PH_3 changes the HOMO (−6.62 eV) and LUMO (−3.27 eV) energies in such a way that a negligible decrease in the $E_{H\text{-}L}$ gap (3.35 eV) is observed for the PH_3@C_6N_6 complex. Among the studied analyte@C_6N_6 complexes, the highest decrease in the $E_{H\text{-}L}$ gap is observed for NH_3@C_6N_6. This indicates that C_6N_6 can act as potential surface for this analyte. Thus, it is concluded that C_6N_6 is highly selective towards NH_3 compared to the other studied analytes.

After adsorption of industrial pollutants (HCN, H_2S, NH_3 and PH_3) onto C_6N_6, the dispersal of orbitals densities was also explored in order to comprehend the sensing abilities of C_6N_6. We observed three types of orbital distribution patterns. In the case of the HCN@C_6N_6 complex, the orbital densities are localized on the triazine ring. In the HOMO, the orbital densities are observed on the carbon and nitrogen of the triazine ring, while in the LUMO, the orbital densities are shifted to the carbon of the triazine ring. This shows that analytes do not participate in the electronic shift from the HOMO to the LUMO (see Figure 7).

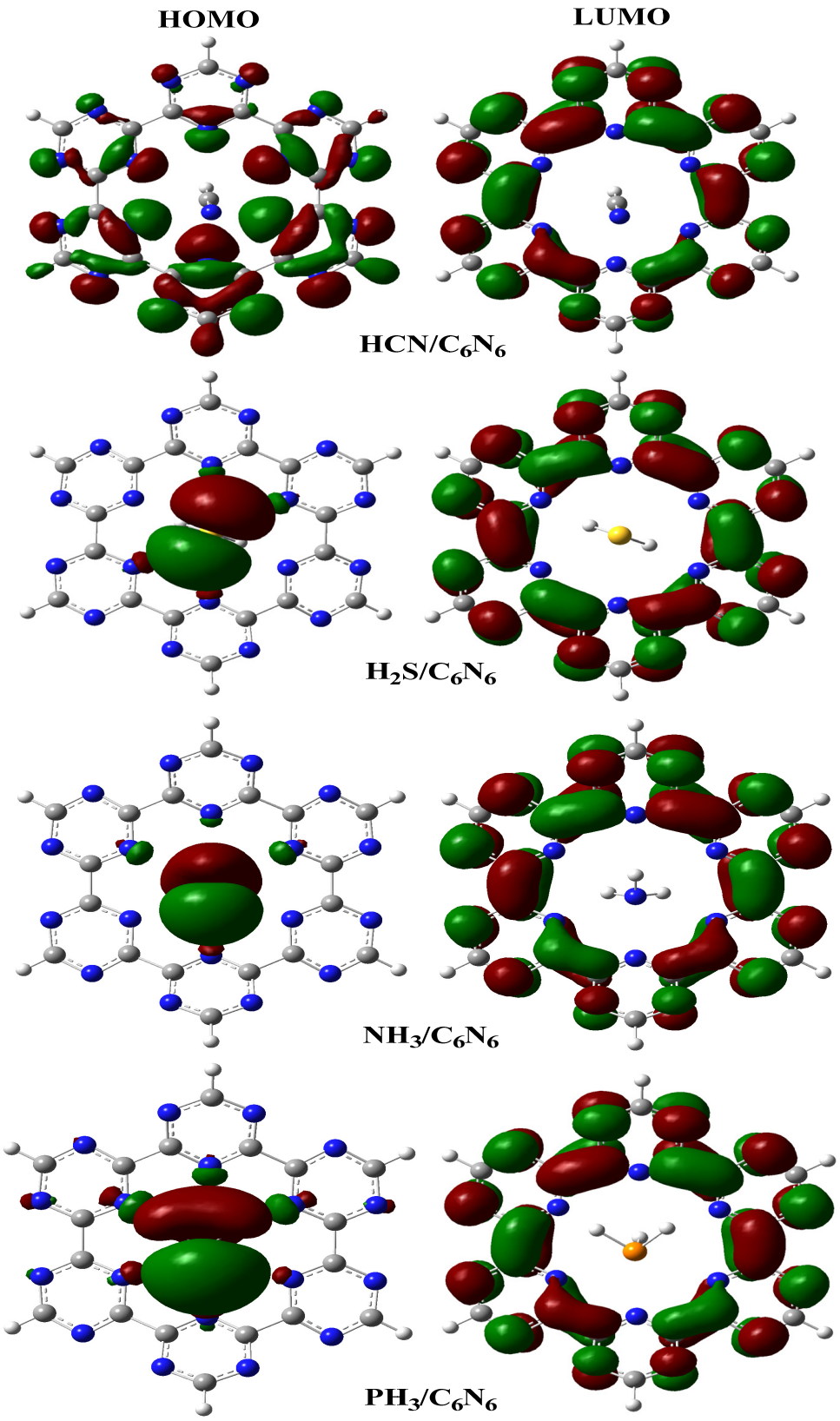

Figure 7. Orbital distribution pattern of analyte@C_6N_6 complexes computed through a FMO analysis (isovalue = 0.02 a.u.). Green orbital densities indicate a positive wavefunction, while red orbital densities show a negative wavefunction.

The intra shift of electronic orbital densities causes an increase in the $E_{H\text{-}L}$ gap compared to bare C_6N_6. In $H_2S@C_6N_6$ and $PH_3@C_6N_6$ complexes, the major portion of the HOMO density is located on the analyte, with some sharing with the N atoms of C_6N_6, while the LUMO density is completely shifted onto C_6N_6. Such a type of electronic transition causes a significant change in the $E_{H\text{-}L}$ gap. A third type of electronic transition is observed in the $NH_3@C_6N_6$ complex, where the HOMO is completely located on NH_3, while the LUMO is shifted to C_6N_6 (see Figure 7). Such a type of electronic transition brings about a significant change in the $E_{H\text{-}L}$ gap. The same sort of behaviour was observed by us previously in a study of the same analytes over C_2N. The transition of orbital density from analytes to the C_2N surface causes considerable changes in the $E_{H\text{-}L}$ gaps [34,71,72].

We compared the adsorption energies of our studied system with those available in the literature for different COFs. The adsorption energies of H-containing analytes are comparable or somewhat higher than already reported values on other surfaces. An adsorption energy of −12.27 kcal/mol is observed for the $NH_3@C_6N_6$ complex, whereas in the literature, adsorption energies of −5.27 kcal/mol, −10.68 kcal/mol and −6.65 kcal/mol are observed for NH_3@CTF-FUM, $NH_3@C_2N$ and NH_3@CTF-0 complexes, respectively. In addition, interaction energies of −15.24 kcal/mol, −3.79 kcal/mol and −2.34 kcal/mol are observed for HCN@CTF-FUM, H_2S@CTF-FUM and PH_3@CTF-FUM, respectively. The adsorption energies of the rest of the complexes are given in Table 4 and reveal that C_6N_6 can act as a better surface for electrochemical sensing of H-containing analytes.

Table 4. Comparison of adsorption energy of H-containing industrial pollutants over C_6N_6 with already reported values of different analytes over C_6N_6 and other COFs.

S.No	Complexes	E_{ads} (kcal/mol)	Ref	S.No	Complexes	E_{ads} (kcal/mol)	Ref
1	NH_3@CTF-FUM	−5.27	[5]	8	HCN@CTF-0	−5.99	[86]
2	H_2S@CTF-FUM	−3.79		9	H_2S@CTF-0	−5.46	
3	PH_3@CTF-FUM	−2.43		10	NH_3@CTF-0	−6.65	
4	$HCN@C_2N$	−15.24	current work	$HCN@C_6N_6$		−16.46	current work
5	$NH_3@C_2N$	−10.68		$PH_3@C_6N_6$		−13.64	
6	$H_2S@C_2N$	−8.54		$NH_3@C_6N_6$		−12.27	
7	$PH_3@C_2N$	−6.91		$PH_3@C_6N_6$		−9.36	

5. Conclusions

The electrochemical sensing application of C_6N_6 is evaluated by DFT simulations at the wb97xd/6-31g(d,p) level of theory. The adsorption of industrial pollutants over C_6N_6 occurred through physisorption, with adsorption energies ranging from −9.36 kcal/mol to −16.46 kcal/mol. Among the considered analytes, the maximum energy is observed for $HCN@C_6N_6$ (−16.46 kcal/mol). The non-covalent interactions of analyte@C_6N_6 complexes are explored through symmetry-adapted perturbation theory (SAPT0), quantum theory of atoms in molecules (QTAIM) analyses and non-covalent interaction (NCI) analyses. The attractive components in SAPT0 analyses show that electrostatic and dispersive interactions play a dominant role in the stabilization of analytes in the C_6N_6 cavity. Similarly, NCI and QTAIM analyses also verified the findings of SAPT0 and interaction energy analyses. In addition, the electron density (ρ_{BCP}) and Laplacian of electron density ($\nabla^2\rho_{bcp}$) remained high for the $HCN@C_6N_6$ complex, which is consistent with the NCI and SAPT0 results. The electronic properties of analyte@C_6N_6 complexes are investigated by electron density difference (EDD), natural bond orbital analyses (NBO) and frontier molecular orbital analyses (FMO). Charge is transferred from the C_6N_6 sheet to HCN, H_2S, NH_3 and PH_3. The highest exchange of charge is noted for H_2S ($-0.026\ e^-$). The results of FMO analyses show that the interaction of all analytes results in changes in the $E_{H\text{-}L}$ gap of the C_6N_6 sheet. However, the highest decrease in the $E_{H\text{-}L}$ gap (2.58 eV) is observed for the $NH_3@C_6N_6$

complex compared to other studied analyte@C_6N_6 complexes. The orbital density pattern shows that the HOMO density is completely concentrated on NH_3, while the LUMO density is transferred towards C_6N_6. This indicates that C_6N_6 can act as potential surface for these analytes. Hence, which analyte is more selective towards C_6N_6 depends on its electrical conductivity and not its adsorption. Thus, it is concluded that C_6N_6 is highly selective towards NH_3 compared to the other studied analytes.

Supplementary Materials: The following supporting information can be downloaded at: https://www.mdpi.com/article/10.3390/nano13061121/s1, Figure S1 caption: Optimized geometries of least stable complexes of each analyte over C6N6 at ωb97XD/6-31G (d,p) level of theory.(HCN/C6N6 complexes (A-C), H2S/C6N6 complexes (D-F), NH3/C6N6 complexes (G-I), PH3/C6N6 complexes (J).

Author Contributions: Conceptualization, M.Y. and H.H.H.; methodology, K.A.; software, K.A.; validation, K.A. and I.B.; formal analysis, I.B.; investigation, M.Y.; resources, H.H.H.; data curation, M.Y.; writing—original draft preparation, H.H.H. and M.Y.; writing—review and editing, K.A.; visualization, M.Y.; supervision, H.H.H. and K.A.; project administration, H.H.H.; funding acquisition, H.H.H. All authors have read and agreed to the published version of the manuscript.

Funding: This research work was funded by the Deputyship for Research and Innovation, Ministry of Education in Saudi Arabia, project number INST158.

Acknowledgments: The authors extend their appreciation to the Deputyship for Research and Innovation, Ministry of Education in Saudi Arabia, for funding this research work (project number INST158).

Conflicts of Interest: The authors declare no conflict of interest.

References

1. Laplaza, R.; Peccati, F.; Boto, R.A.; Quan, C.; Carbone, A.; Piquemal, J.P.; Maday, Y.; Contreras-García, J. NCIPLOT and the Analysis of Noncovalent Interactions Using the Reduced Density Gradient. *Wiley Interdiscip. Rev. Comput. Mol. Sci.* **2021**, *11*, e1497. [CrossRef]
2. Wang, Y.; Ning, P.; Zhao, R.; Li, K.; Wang, C.; Sun, X.; Song, X.; Lin, Q. A Cu-Modified Active Carbon Fiber Significantly Promoted H_2S and PH_3 Simultaneous Removal at a Low Reaction Temperature. *Front. Environ. Sci. Eng.* **2021**, *15*, 132. [CrossRef]
3. Haridas, V.; Sukhananazerin, A.; Sneha, J.M.; Pullithadathil, B.; Narayanan, B. α-Fe_2O_3 Loaded Less-Defective Graphene Sheets as Chemiresistive Gas Sensor for Selective Sensing of NH_3. *Appl. Surf. Sci.* **2020**, *517*, 146158. [CrossRef]
4. Farooqi, B.A.; Yar, M.; Ashraf, A.; Farooq, U.; Ayub, K. Polyaniline emeraldine salt as selective electrochemical sensor for HBr over HCl: A systematic density functional theory study through oligomer approach. *J. Mol. Model.* **2020**, *26*, 332. [CrossRef] [PubMed]
5. Khan, S.; Yar, M.; Kosar, N.; Ayub, K.; Arshad, M.; Zahid, N.; Mahmood, T. First-principles study for exploring the adsorption behavior of G-series nerve agents on graphdyine surface. *Comput. Theor. Chem.* **2020**, *1191*, 113043. [CrossRef]
6. Matthews, C.N. Dark Matter in the Solar System: Hydrogen Cyanide Polymers. *Orig. Life Evol. Biosph.* **1991**, *21*, 421–434. [CrossRef]
7. Ding, Y.; Li, X.; Chen, C.; Ling, J.; Li, W.; Guo, Y.; Yan, J.; Zha, L.; Cai, J. A Rapid Evaluation of Acute Hydrogen Sulfide Poisoning in Blood Based on DNA-Cu/Ag Nanocluster Fluorescence Probe. *Sci. Rep.* **2017**, *7*, 9638. [CrossRef]
8. Lemus, J.; Bedia, J.; Moya, C.; Alonso-Morales, N.; Gilarranz, M.A.; Palomar, J.; Rodriguez, J.J. Ammonia Capture from the Gas Phase by Encapsulated Ionic Liquids (ENILs). *RSC Adv.* **2016**, *6*, 61650–61660. [CrossRef]
9. Bai, Z.; Dong, Y.; Wang, Z.; Zhu, T. Emission of Ammonia from Indoor Concrete Wall and Assessment of Human Exposure. *Environ. Int.* **2006**, *32*, 303–311. [CrossRef]
10. Nath, N.S.; Bhattacharya, I.; Tuck, A.G.; Schlipalius, D.I.; Ebert, P.R. Mechanisms of Phosphine Toxicity. *J. Toxicol.* **2011**, *2011*, 494168. [CrossRef]
11. Zhou, X.; Su, Z.; Chen, H.; Xiao, X.; Qin, Y.; Yang, L.; Yan, Z.; Sun, W. Capture of Pure Toxic Gases through Porous Materials from Molecular Simulations. *Mol. Phys.* **2018**, *116*, 2095–2107. [CrossRef]
12. Li, J.-R.; Kuppler, R.J.; Zhou, H.-C. Selective Gas Adsorption and Separation in Metal–Organic Frameworks. *Chem. Soc. Rev.* **2009**, *38*, 1477. [CrossRef] [PubMed]
13. Yar, M.; Ahsan, F.; Gulzar, A.; Ayub, K. Adsorption and Sensor Applications of C_2N Surface for G-Series and Mustard Series Chemical Warfare Agents. *Microporous Mesoporous Mater.* **2021**, *317*, 110984. [CrossRef]
14. He, Y.; Li, D.; Gao, W.; Yin, H.; Chen, F.; Sun, Y. High-Performance NO2 Sensors based on Spontaneously Functionalized Hexagonal Boron Nitride Nanosheets via Chemical Exfoliation. *Nanoscale* **2019**, *11*, 21909–21916. [CrossRef]
15. Wang, C.; Yin, L.; Zhang, L.; Xiang, D.; Gao, R. Metal Oxide Gas Sensors: Sensitivity and Influencing Factors. *Sensors* **2010**, *10*, 2088–2106. [CrossRef] [PubMed]

16. Lu, G.; Hupp, J.T. Metal−Organic Frameworks as Sensors: A ZIF-8 Based Fabry−Pérot Device as a Selective Sensor for Chemical Vapors and Gases. *J. Am. Chem. Soc.* **2010**, *132*, 7832–7833. [CrossRef]
17. Rowsell, J.L.C.; Yaghi, O.M. Effects of Functionalization, Catenation, and Variation of the Metal Oxide and Organic Linking Units on the Low-Pressure Hydrogen Adsorption Properties of Metal−Organic Frameworks. *J. Am. Chem. Soc.* **2006**, *128*, 1304–1315. [CrossRef]
18. Rostami, Z.; Soleymanabadi, H. Investigation of Phosgene Adsorption Behavior on Aluminum Nitride Nanocones: Density Functional Study. *J. Mol. Liq.* **2017**, *248*, 473–478. [CrossRef]
19. Deng, Z.-Y.; Zhang, J.-M.; Xu, K.-W. Adsorption of SO_2 Molecule on Doped (8, 0) Boron Nitride Nanotube: A First-Principles Study. *Phys. E Low Dimens. Syst. Nanostruct.* **2016**, *76*, 47–51. [CrossRef]
20. Broitman, E.; Gueorguiev, G.K.; Furlan, A.; Son, N.T.; Gellman, A.J.; Stafström, S.; Hultman, L. Water Adsorption on Fullerene-like Carbon Nitride Overcoats. *Thin Solid Films* **2008**, *517*, 1106–1110. [CrossRef]
21. Yuan, J.; Li, G.; Yang, B.; Zhang, J.; Li, Z.; Chen, H. Selective Adsorption of Ethylene on Bimetallic CuVn+/0 (n = 1–5) Clusters: A Theoretical Study. *Comput. Mater. Sci.* **2016**, *111*, 489–496. [CrossRef]
22. Broitman, E.; Furlan, A.; Gueorguiev, G.K.; Czigány, Z.; Tarditi, A.M.; Gellman, A.J.; Stafström, S.; Hultman, L. Water Adsorption on Phosphorous-Carbide Thin Films. *Surf. Coat. Technol.* **2009**, *204*, 1035–1039. [CrossRef]
23. Korotcenkov, G. Metal Oxides for Solid-State Gas Sensors: What Determines Our Choice? *Mater. Sci. Eng. B* **2007**, *139*, 1–23. [CrossRef]
24. Sahoo, H.R.; Kralj, J.G.; Jensen, K.F. Multistep Continuous-Flow Microchemical Synthesis Involving Multiple Reactions and Separations. *Angew. Chemie Int. Ed.* **2007**, *46*, 5704–5708. [CrossRef] [PubMed]
25. Sangiovanni, D.G.; Gueorguiev, G.K.; Kakanakova-Georgieva, A. Ab Initio Molecular Dynamics of Atomic-Scale Surface Reactions: Insights into Metal Organic Chemical Vapor Deposition of AlN on Graphene. *Phys. Chem. Chem. Phys.* **2018**, *20*, 17751–17761. [CrossRef]
26. Anota, E.C.; Juárez, A.R.; Castro, M.; Cocoletzi, H.H. A Density Functional Theory Analysis for the Adsorption of the Amine Group on Graphene and Boron Nitride Nanosheets. *J. Mol. Model.* **2013**, *19*, 321–328. [CrossRef]
27. Limon, P.; Miralrio, A.; Castro, M. Adsorption and Dissociation of Carbon Monoxide on Iron and Iron-Carbon Clusters: Fen + 2CO and FenC + 2CO, N = 4 and 7. A Theoretical Study. *Comput. Theor. Chem.* **2018**, *1129*, 37–47. [CrossRef]
28. Online, V.A. RSC Advances Long Range Corrected-WPBE Based Analysis of the H_2O Adsorption on Magnetic BC_3 Nanosheets. *RSC Adv.* **2016**, *6*, 20409–20421. [CrossRef]
29. Baughman, R.H. Carbon Nanotubes—The Route Toward Applications. *Science* **2002**, *297*, 787–792. [CrossRef]
30. Rafiee, M.A.; Rafiee, J.; Wang, Z.; Song, H.; Yu, Z.-Z.; Koratkar, N. Enhanced Mechanical Properties of Nanocomposites at Low Graphene Content. *ACS Nano* **2009**, *3*, 3884–3890. [CrossRef]
31. Yang, X.; Cheng, C.; Wang, Y.; Qiu, L.; Li, D. Liquid-Mediated Dense Integration of Graphene Materials for Compact Capacitive Energy Storage. *Science* **2013**, *341*, 534–537. [CrossRef] [PubMed]
32. Ni, Z.; Liu, Q.; Tang, K.; Zheng, J.; Zhou, J.; Qin, R.; Gao, Z.; Yu, D.; Lu, J. Tunable Bandgap in Silicene and Germanene. *Nano Lett.* **2012**, *12*, 113–118. [CrossRef] [PubMed]
33. Wang, Q.H.; Kalantar-Zadeh, K.; Kis, A.; Coleman, J.N.; Strano, M.S. Electronics and Optoelectronics of Two-Dimensional Transition Metal Dichalcogenides. *Nat. Nanotechnol.* **2012**, *7*, 699–712. [CrossRef] [PubMed]
34. Xu, M.; Liang, T.; Shi, M.; Chen, H. Graphene-Like Two-Dimensional Materials. *Chem. Rev.* **2013**, *113*, 3766–3798. [CrossRef]
35. Vogt, P.; De Padova, P.; Quaresima, C.; Avila, J.; Frantzeskakis, E.; Asensio, M.C.; Resta, A.; Ealet, B.; Le Lay, G. Silicene: Compelling Experimental Evidence for Graphenelike Two-Dimensional Silicon. *Phys. Rev. Lett.* **2012**, *108*, 155501. [CrossRef] [PubMed]
36. Jose, D.; Datta, A. Structures and Chemical Properties of Silicene: Unlike Graphene. *Acc. Chem. Res.* **2014**, *47*, 593–602. [CrossRef]
37. Liu, H.; Neal, A.T.; Zhu, Z.; Luo, Z.; Xu, X.; Tománek, D.; Ye, P.D. Phosphorene: An Unexplored 2D Semiconductor with a High Hole Mobility. *ACS Nano* **2014**, *8*, 4033–4041. [CrossRef]
38. Meric, I.; Han, M.Y.; Young, A.F.; Ozyilmaz, B.; Kim, P.; Shepard, K.L. Current Saturation in Zero-Bandgap, Top-Gated Graphene Field-Effect Transistors. *Nat. Nanotechnol.* **2008**, *3*, 654–659. [CrossRef]
39. Zhang, Y.-H.; Chen, Y.-B.; Zhou, K.-G.; Liu, C.-H.; Zeng, J.; Zhang, H.-L.; Peng, Y. Improving Gas Sensing Properties of Graphene by Introducing Dopants and Defects: A First-Principles Study. *Nanotechnology* **2009**, *20*, 185504. [CrossRef]
40. Wang, X.; Sun, G.; Routh, P.; Kim, D.-H.; Huang, W.; Chen, P. Heteroatom-Doped Graphene Materials: Syntheses, Properties and Applications. *Chem. Soc. Rev.* **2014**, *43*, 7067–7098. [CrossRef]
41. Zhang, W.; Lin, C.-T.; Liu, K.-K.; Tite, T.; Su, C.-Y.; Chang, C.-H.; Lee, Y.-H.; Chu, C.-W.; Wei, K.-H.; Kuo, J.-L.; et al. Opening an Electrical Band Gap of Bilayer Graphene with Molecular Doping. *ACS Nano* **2011**, *5*, 7517–7524. [CrossRef]
42. Cote, A.P. Porous, Crystalline, Covalent Organic Frameworks. *Science* **2005**, *310*, 1166–1170. [CrossRef]
43. Ma, H.; Liu, B.; Li, B.; Zhang, L.; Li, Y.-G.; Tan, H.-Q.; Zang, H.-Y.; Zhu, G. Cationic Covalent Organic Frameworks: A Simple Platform of Anionic Exchange for Porosity Tuning and Proton Conduction. *J. Am. Chem. Soc.* **2016**, *138*, 5897–5903. [CrossRef]
44. Ning, G.-H.; Liu, C.; Loh, K.P.; Leng, K.; Tang, W.; Gao, Q.; Xu, H.-S.; Tian, B.; Li, X. Highly Photoluminescent Two-Dimensional Imine-Based Covalent Organic Frameworks for Chemical Sensing. *Chem. Commun.* **2018**, *54*, 2349–2352. [CrossRef]

45. Zhu, M.W.; Xu, S.Q.; Wang, X.Z.; Chen, Y.; Dai, L.; Zhao, X. The Construction of Fluorescent Heteropore Covalent Organic Frameworks and Their Applications in Spectroscopic and Visual Detection of Trinitrophenol with High Selectivity and Sensitivity. *Chem. Commun.* **2018**, *54*, 2308–2311. [CrossRef]
46. Cui, F.; Liang, R.; Qi, Q.; Jiang, G.; Zhao, X. Efficient Removal of Cr(VI) from Aqueous Solutions by a Dual-Pore Covalent Organic Framework. *Adv. Sustain. Syst.* **2019**, *3*, 1800150. [CrossRef]
47. Jansone-Popova, S.; Moinel, A.; Schott, J.A.; Mahurin, S.M.; Popovs, I.; Veith, G.M.; Moyer, B.A. Guanidinium-Based Ionic Covalent Organic Framework for Rapid and Selective Removal of Toxic Cr(VI) Oxoanions from Water. *Environ. Sci. Technol.* **2019**, *53*, 878–883. [CrossRef]
48. Jiang, Q.; Huang, H.; Tang, Y.; Zhang, Y.; Zhong, C. Highly Porous Covalent Triazine Frameworks for Reversible Iodine Capture and Efficient Removal of Dye. *Ind. Eng. Chem. Res.* **2018**, *57*, 15114–15121. [CrossRef]
49. Fayyaz, F.; Yar, M.; Gulzar, A.; Ayub, K. First principles calculations of the adsorption of fluorouracil and nitrosourea on CTF-0; organic frameworks as drug delivery systems for cancer treatment. *J. Mol. Liq.* **2022**, *356*, 118941. [CrossRef]
50. Liao, L.; Li, M.; Yin, Y.; Chen, J.; Zhong, Q.; Du, R.; Liu, S.; He, Y.; Fu, W.; Zeng, F. Advances in the Synthesis of Covalent Triazine Frameworks. *ACS Omega* **2023**, *8*, 4527–4542. [CrossRef]
51. Sarfaraz, S.; Yar, M.; Ans, M.; Gilani, M.A.; Ludwig, R.; Hashmi, M.A.; Hussain, M.; Muhammad, S.; Ayub, K. Computational Investigation of a Covalent Triazine Framework (CTF-0) as an Efficient Electrochemical Sensor. *RSC Adv.* **2022**, *12*, 3909–3923. [CrossRef] [PubMed]
52. Yang, K.; Yuan, W.; Hua, Z.; Tang, Y.; Yin, F.; Xia, D. Triazine-Based Two-Dimensional Organic Polymer for Selective NO_2 Sensing with Excellent Performance. *ACS Appl. Mater. Interfaces* **2020**, *12*, 3919–3927. [CrossRef] [PubMed]
53. Liu, M.; Guo, L.; Jin, S.; Tan, B. Covalent Triazine Frameworks: Synthesis and Applications. *J. Mater. Chem. A* **2019**, *7*, 5153–5172. [CrossRef]
54. Liang, D.; Jing, T.; Ma, Y.; Hao, J.; Sun, G.; Deng, M. Photocatalytic Properties of G-C_6N_6/g-C_3N_4 Heterostructure: A Theoretical Study. *J. Phys. Chem. C* **2016**, *120*, 24023–24029. [CrossRef]
55. Zhang, W.X.; Yan, H.M.; He, C. G-C_6N_6 Monolayer: A Highly Sensitive Molecule Sensor for Biomarker Volatiles of Liver Cirrhosis. *Appl. Surf. Sci.* **2021**, *566*, 150716. [CrossRef]
56. Alkhalifah, M.A.; Yar, M.; Bayach, I.; Sheikh, N.S.; Ayub, K. Covalent Organic Framework (C_6N_6) as a Drug Delivery Platform for Fluorouracil to Treat Cancerous Cells: A DFT Study. *Materials* **2022**, *15*, 7425. [CrossRef]
57. Bafekry, A.; Stampfl, C.; Akgenc, B.; Mortazavi, B.; Ghergherehchi, M.; Nguyen, C.V. Embedding of Atoms into the Nanopore Sites of the C_6N_6 and C_6N_8 Porous Carbon Nitride Monolayers with Tunable Electronic Properties. *Phys. Chem. Chem. Phys.* **2020**, *22*, 6418–6433. [CrossRef]
58. Pagliai, M.; Caporali, S.; Muniz-Miranda, M.; Pratesi, G.; Schettino, V. SERS, XPS, and DFT Study of Adenine Adsorption on Silver and Gold Surfaces. *J. Phys. Chem. Lett.* **2012**, *3*, 242–245. [CrossRef]
59. Chai, J.-D.; Head-Gordon, M. Long-Range Corrected Hybrid Density Functionals with Damped Atom–Atom Dispersion Corrections. *Phys. Chem. Chem. Phys.* **2008**, *10*, 6615. [CrossRef]
60. Zhang, H.-J.; Qi, S.-D.; Niu, X.-Y.; Hu, J.; Ren, C.-L.; Chen, H.-L.; Chen, X.-G. Metallic nanoparticles immobilized in magnetic metal-organic frameworks: Preparation and application as highly active, magnetically isolable and reusable catalysts. *Catal. Sci. Technol.* **2014**, *4*, 3013–3024. [CrossRef]
61. Yar, M.; Ayub, K. Expanding the Horizons of Covalent Organic Frameworks to Electrochemical Sensors; A Case Study of CTF-FUM. *Microporous Mesoporous Mater.* **2020**, *300*, 110146. [CrossRef]
62. Farooqi, B.A.; Yar, M.; Ashraf, A.; Farooq, U.; Ayub, K. Graphene-Polyaniline Composite as Superior Electrochemical Sensor for Detection of Cyano Explosives. *Eur. Polym. J.* **2020**, *138*, 109981. [CrossRef]
63. Yar, M.; Hashmi, M.A.; Ayub, K. Nitrogenated Holey Graphene (C_2N) Surface as Highly Selective Electrochemical Sensor for Ammonia. *J. Mol. Liq.* **2019**, *296*, 111929. [CrossRef]
64. Yar, M.; Hashmi, M.A.; Ayub, K. The C_2N Surface as a Highly Selective Sensor for the Detection of Nitrogen Iodide from a Mixture of NX_3 (X = Cl, Br, I) Explosives. *RSC Adv.* **2020**, *10*, 31997–32010. [CrossRef]
65. Kazachenko, A.S.; Tomilin, F.N.; Pozdnyakova, A.A.; Vasilyeva, N.Y.; Malyar, Y.N.; Kuznetsova, S.A.; Avramov, P.V. Theoretical DFT Interpretation of Infrared Spectra of Biologically Active Arabinogalactan Sulphated Derivatives. *Chem. Pap.* **2020**, *74*, 4103–4113. [CrossRef]
66. Jeziorski, B.; Moszynski, R.; Szalewicz, K. Perturbation Theory Approach to Intermolecular Potential Energy Surfaces of van Der Waals Complexes. *Chem. Rev.* **1994**, *94*, 1887–1930. [CrossRef]
67. Pan, S.; Saha, R.; Mandal, S.; Mondal, S.; Gupta, A.; Fernández-Herrera, M.A.; Merino, G.; Chattaraj, P.K. Selectivity in Gas Adsorption by Molecular Cucurbit[6]Uril. *J. Phys. Chem. C* **2016**, *120*, 13911–13921. [CrossRef]
68. Keinan, S.; Contreras-García, J.; Johnson, E.R.; Yang, W.; Mori-Sánchez, P.; Cohen, A.J. Revealing Noncovalent Interactions. *J. Am. Chem. Soc.* **2010**, *132*, 6498–6506. [CrossRef]
69. Contreras-García, J.; Johnson, E.R.; Keinan, S.; Chaudret, R.; Piquemal, J.-P.; Beratan, D.N.; Yang, W. NCIPLOT: A Program for Plotting Noncovalent Interaction Regions. *J. Chem. Theory Comput.* **2011**, *7*, 625–632. [CrossRef]
70. Contreras-García, J.; Yang, W.; Johnson, E.R. Analysis of Hydrogen-Bond Interaction Potentials from the Electron Density: Integration of Noncovalent Interaction Regions. *J. Phys. Chem. A* **2011**, *115*, 12983–12990. [CrossRef]

71. Venkataramanan, N.S.; Suvitha, A.; Kawazoe, Y. Unravelling the Nature of Binding of Cubane and Substituted Cubanes within Cucurbiturils: A DFT and NCI Study. *J. Mol. Liq.* **2018**, *260*, 18–29. [CrossRef]
72. Mohammadi, M.D.; Abdullah, H.Y. The Adsorption of Chlorofluoromethane on Pristine, Al-, Ga-, P-, and As-Doped Boron Nitride Nanotubes: A PBC-DFT, NBO, and QTAIM Study. *ChemistrySelect* **2020**, *5*, 12115–12124. [CrossRef]
73. Chu, Z.Q.; Stampfl, C.; Duan, X.M. Boron-Doped g-C_6N_6 Layer as a Metal-Free Photoelectrocatalyst for N_2 Reduction Reaction. *J. Phys. Chem. C* **2019**, *123*, 28739–28743. [CrossRef]
74. Wang, L.; Liu, Y.-L.; Wang, M.-S. Effects of Atypical Hydrogen Bonds and π–π Interactions on Nonlinear Optical Properties: Dimers of Triangular Structures Based on Perylene, Naphthalene, and Pyromellitic Diimides. *Langmuir* **2022**, *39*, 357–366. [CrossRef]
75. Lu, T.; Chen, F. Quantitative analysis of molecular surface based on improved Marching Tetrahedra algorithm. *J. Mol. Graph. Model.* **2012**, *38*, 314–323. [CrossRef] [PubMed]
76. Munir, M.; Ahsan, F.; Yar, M.; Ayub, K. Theoretical Investigation of Double-Cubed Polycationic Cluster (Sb7Se8Cl2)3+ for the Storage of Helium and Neon. *Mater. Sci. Semicond. Process.* **2022**, *148*, 106756. [CrossRef]
77. Srinivasu, K.; Modak, B.; Ghosh, S.K. Porous Graphitic Carbon Nitride: A Possible Metal-Free Photocatalyst for Water Splitting. *J. Phys. Chem. C* **2014**, *118*, 26479–26484. [CrossRef]
78. Li, T.; Zhang, W.-D.; Liu, Y.; Li, Y.; Cheng, C.; Zhu, H.; Yan, X.; Li, Z.; Gu, Z.-G. A Two-Dimensional Semiconducting Covalent Organic Framework with Nickel(ii) Coordination for High Capacitive Performance. *J. Mater. Chem. A* **2019**, *7*, 19676–19681. [CrossRef]
79. Trendafilova, N.; Bauer, G.; Mihaylov, T. DFT and AIM Studies of Intramolecular Hydrogen Bonds in Dicoumarols. *Chem. Phys.* **2004**, *302*, 95–104. [CrossRef]
80. Ghogomu, J.N.; Nkungli, N.K. DFT Studies and Topological Analyses of Electron Density on Acetophenone and Propiophenone Thiosemicarbazone Derivatives as Covalent Inhibitors of Falcipain-2, a Major Plasmodium Falciparum Cysteine Protease. *Phys. Chem. Res* **2017**, *5*, 795–817. [CrossRef]
81. Alkorta, I.; Elguero, J.; Solimannejad, M.; Grabowski, S.J. Dihydrogen Bonding vs Metal−σ Interaction in Complexes between H_2 and Metal Hydride. *J. Phys. Chem. A* **2011**, *115*, 201–210. [CrossRef]
82. Espinosa, E.; Molins, E.; Lecomte, C. Hydrogen Bond Strengths Revealed by Topological Analyses of Experimentally Observed Electron Densities. *Chem. Phys. Lett.* **1998**, *285*, 170–173. [CrossRef]
83. Steiner, T. The Hydrogen Bond in the Solid State. *Angew. Chemie Int. Ed.* **2002**, *41*, 48–76. [CrossRef]
84. Cremer, D.; Kraka, E. Theoretical Determination of Molecular Structure and Conformation. 15. Three-Membered Rings: Bent Bonds, Ring Strain, and Surface Delocalization. *J. Am. Chem. Soc.* **1985**, *107*, 3800–3810. [CrossRef]
85. Du, J.; Sun, X.; Jiang, G. Exploring the Interaction Natures in Plutonyl (VI) Complexes with Topological Analyses of Electron Density. *Int. J. Mol. Sci.* **2016**, *17*, 414. [CrossRef]
86. Sarfaraz, S.; Yar, M.; Ayub, K. Covalent Triazine Framework (CTF-0) Surface as a Smart Sensing Material for the Detection of CWAs and Industrial Pollutants. *Mater. Sci. Semicond. Process.* **2022**, *139*, 106334. [CrossRef]